



HAL
open science

Phase Diagram of BiFeO₃ /LaFeO₃ Superlattices: Antiferroelectric-Like State Stability Arising from Strain Effects and Symmetry Mismatch at Heterointerfaces

Benjamin Carcan, Houssny Bouyanfif, Mimoun El Marssi, Françoise Le Marrec, Loic Dupont, Carine Davoisne, Jérôme Wolfman, Donna Arnold

► To cite this version:

Benjamin Carcan, Houssny Bouyanfif, Mimoun El Marssi, Françoise Le Marrec, Loic Dupont, et al.. Phase Diagram of BiFeO₃ /LaFeO₃ Superlattices: Antiferroelectric-Like State Stability Arising from Strain Effects and Symmetry Mismatch at Heterointerfaces. *Advanced Materials Interfaces*, 2017, 4 (11), 10.1002/admi.201601036 . hal-01867383

HAL Id: hal-01867383

<https://univ-tours.hal.science/hal-01867383>

Submitted on 10 Sep 2018

HAL is a multi-disciplinary open access archive for the deposit and dissemination of scientific research documents, whether they are published or not. The documents may come from teaching and research institutions in France or abroad, or from public or private research centers.

L'archive ouverte pluridisciplinaire **HAL**, est destinée au dépôt et à la diffusion de documents scientifiques de niveau recherche, publiés ou non, émanant des établissements d'enseignement et de recherche français ou étrangers, des laboratoires publics ou privés.

Interlayer strain effects on the structural behavior of BiFeO₃/LaFeO₃ superlattices

B. Carcan¹, H. Bouyanfif^{1,*}, M. El Marssi¹, F. Le Marrec¹, L. Dupont^{2,3}, C. Davoisne²,

J. Wolfman⁴, D. C. Arnold⁵

¹LPMC EA2081, Université de Picardie Jules Verne, 33 Rue Saint Leu,

80039 Amiens, France

²LRCS UMR7314, Université de Picardie Jules Verne,

33 Rue Saint Leu, 80039 Amiens, France

³Plateforme de microscopie électronique, Université de Picardie Jules Verne,

33 Rue Saint Leu, 80039 Amiens, France

⁴GREMAN UMR7347, Université de Tours François Rabelais, 20 Avenue Monge,

37200 Tours, France

⁵School of Physical Sciences, University of Kent, Canterbury, Kent, CT2 7NH, UK

Abstract

Artificial (BiFeO₃)_{0.5Λ}/(LaFeO₃)_{0.5Λ} superlattices (SLs) have been grown by pulsed laser deposition. The periodicity Λ was varied from 150 Å to 25 Å and the relative ratio between BFO and LFO is kept constant in each period. X-ray diffraction, transmission electron microscopy (TEM) and Raman spectroscopy investigations indicate antiferroelectric-like structures for large periodicity ($\Lambda \geq 76$ Å) while Pnma LaFeO₃-like structures are observed for small periodicity $\Lambda \leq 50$ Å. Room temperature Magnetic measurements were obtained by vibrating sample magnetometry and suggest antiferromagnetic ordering with weak ferromagnetism. Temperature dependent x-ray diffraction studies show an important shift

of paraelectric-antiferroelectric phase transition scaling with BFO thickness. Strain and size effects explain this behavior and discussion is also made of the possible role of the oxygen octahedral rotation/tilt degree of freedom.

Introduction

BiFeO_3 (BFO) has attracted enormous interest due to its multiferroic nature at room temperature. Indeed, coexistence of two robust ferroic properties (ferroelectricity with $T_c=830^\circ\text{C}$ and antiferromagnetism with $T_N=370^\circ\text{C}$) paves the way to applications in the field of information storage¹. Important electromechanical properties were also detected in BFO thin films but are unfortunately limited by the high leakage currents. In order to decrease the leakage currents chemical substitutions have been utilized and in particular rare earth substitutions of Bismuth ($\text{Bi}_{1-x}\text{RE}_x\text{FeO}_3$; RE: Sm, Gd, Dy, La) have shown improved physical properties². For some compositions (Sm, Gd, Dy) high piezoelectric responses were observed and linked to a morphotropic phase boundary (MPB) between a rhombohedral $R3c$ phase and an orthorhombic Pnma phase³. Depending on the chemical composition (Sm, Dy or La) and temperature, transmission electron microscopy has allowed for the detection of an incommensurate structure and local ordering with an antiferroelectric (AFE) PbZrO_3 like-state. The exact origin of the MPB is not yet fully understood and is still the subject of intense research^{4,5}.

An original approach to investigate the origin of such MPBs and to probe structural competition is the use of superlattices (SLs) artificial structures. Superlattices are not only ideal platforms for enhancing existing properties but also an original method to obtain emerging exotic properties not found in the individual component. Functional properties such as leakage current and ferroelectric properties were improved by tuning the period in

BiFeO₃/SrTiO₃ SLs⁶. More recently, successful control of the morphotropic boundary has been demonstrated in 200 nm thick (001) oriented BiFeO₃/(Bi_{1-x}Sm_xFeO₃) SLs⁷. BFO/LFO SLs have already been investigated by Rispens *et al.* on orthorhombic DyScO₃ (110)_o substrates and revealed complex functional behavior that strongly depends on the composition and temperature⁸. However, the exact structure of the BFO/LFO, SLs structures was not fully understood in contrast to BFO/(Bi,Sm)FeO₃ SLs in which incommensurate structure and antiferroelectric like ordering were found . However it is difficult to distinguish the effects of chemical alloying from pure superlattices ordering in this last type of structures grown using a combinatorial method (the (Bi,Sm)FeO₃ layers in the superlattices present a continuous variation of composition).

In the present work, SLs approach is used to better understanding the structural competition between BFO and LFO responsible of the MPB. We have artificially introduced in competition BiFeO₃ (3.96 Å is a pseudo cubic unit cell parameter) and LaFeO₃ (3.93 Å) of R3c and Pnma symmetry respectively in bulk. We focus on multilayers of (BiFeO₃)_{0.5Λ} / (LaFeO₃)_{0.5Λ} grown on cubic MgO (100) substrates of about 700 Å total thickness. We have previously shown the possibility to induce an antiferroelectric like state in (BiFeO₃)_{(1-x)Λ} / (LaFeO₃)_{xΛ} superlattices by varying the ratio, x, of the constituent in the period⁹. We adopt here another approach to investigate the structural coupling between BFO and LFO. In order to investigate the coupling between each constituent we varied the number of periods (N= 5 to N=30) (i.e the modulation periods Λ =150 Å to Λ =25 Å) and kept constant the total thickness and quantity of BFO and LFO in the period. In other words, we investigated the effects of the number of interfaces, size and strain on the structure of BFO and LFO in such SLs.

Experimental details

BFO/LFO superlattices were grown on cubic single crystal (100) MgO substrates ($a_{\text{MgO}} = 4.213 \text{ \AA}$) by pulsed laser deposition (MECA 2000 chamber) using KrF laser (248 nm). BFO and LFO layers were grown at the same conditions under 0.3 mbar of oxygen pressure (PO_2) at 750°C at 3Hz repetition rate. To promote epitaxial growth and the perovskite phase, a SrTiO_3 20 nm thick buffer layer was used and deposited at 10^{-5} mbar of PO_2 and 800°C . Unlike other substrates, MgO substrate (Raman inactive) allows us to investigate multilayers by Raman spectroscopy. X-rays diffraction measurements were performed using a high-resolution 4-circles diffractometer with a $\text{Cu K}\lambda_1$ parallel beam (Bruker Discover D8). Transmission electron microscopy (TEM) was performed using an S-TWIN FEI TECNAI F20 microscope on cross sections of samples prepared using a focused ion beam (FIB) technique. Prior to FIB processing a protecting Pt top layer was deposited on the multilayers. Magnetometry was performed using a vibrating sample magnetometer using a cryogen free Quantum Design PPMS. Raman spectroscopy investigations were carried out using the 514.5 nm line from an argon ion laser and analyzed using a Jobin Yvon T64000 spectrometer equipped with a charge coupled device. An optical microscope was used to focus the incident light as a spot of $0.9 \mu\text{m}$ in diameter on the sample (objective x100). Scattered light was collected using the same objective of the microscope (back scattering geometry). Raman spectra were measured in cross ($Z(XY)\bar{Z}$) and parallel ($Z(XX)\bar{Z}$) geometry (Porto notation). X, Y and Z corresponding respectively to [100], [010] and [001] of MgO crystallographic axes.

Results and discussion

Room temperature θ - 2θ X-ray diffraction patterns for the superlattices of $(\text{BiFeO}_3)_{0.5\Lambda}/(\text{LaFeO}_3)_{0.5\Lambda}$ for $25 \text{ \AA} \leq \Lambda \leq 150 \text{ \AA}$ are shown in Figure 1 (a). Regularly spaced satellite peaks (denoted by the asterisks) confirm the synthesis of chemically modulated structures along the growth direction. Moreover, within the limits of our instrument, no parasitic phases are detected and all SLs exhibit epitaxial growth.

For more clarity, X-ray diffraction patterns are also represented between $2\theta = 42^\circ$ and $2\theta = 48^\circ$ in Figure 1 (b). For larger modulation periods $\Lambda \geq 76 \text{ \AA}$, the most intense satellite peak at $2\theta = 45.8^\circ$ is accompanied by a shoulder at $2\theta = 46.15^\circ$ indicating the coexistence of two distinct crystallographic orientations. A change of relative intensity of the two peaks (peak at $2\theta = 46.15^\circ$ more intense than the peak at $2\theta = 45.8^\circ$) is observed at $\Lambda = 50 \text{ \AA}$. These observations suggest that another orientation is favored or a structural change takes place for $76 \text{ \AA} \leq \Lambda \leq 50 \text{ \AA}$. The buffer STO layers (20nm thickness) are not observed presumably because of the very weak diffraction intensity (at 1st order) and the 2nd order diffraction peak (around $2\theta = 46^\circ$) overlaps with the SLs intense peaks.

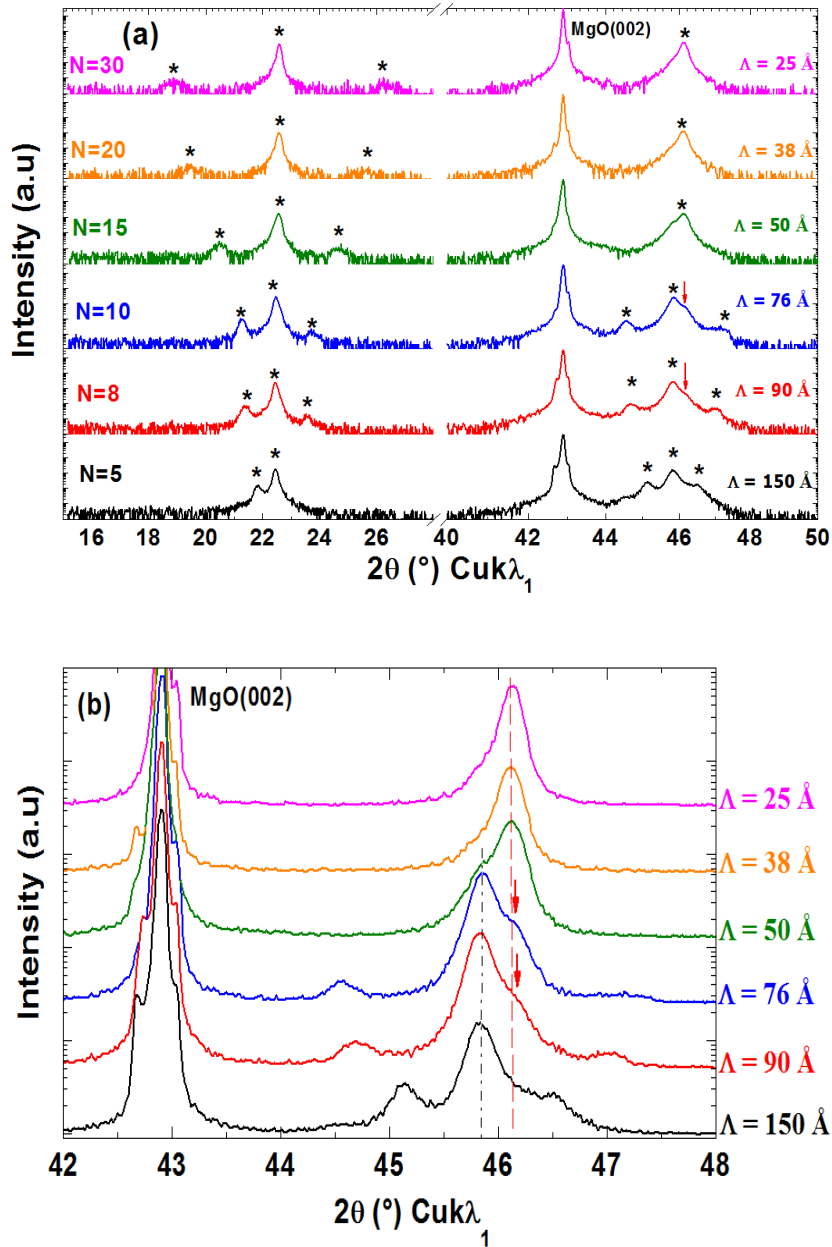


Figure 1: (a) θ - 2θ XRD patterns of $(\text{BiFeO}_3)_{0.5\Lambda} / (\text{LaFeO}_3)_{0.5\Lambda}$ superlattices as a function of modulation periods ($25 \text{ \AA} \leq \Lambda \leq 150 \text{ \AA}$) grown on MgO substrate. Asterisks indicate satellite peaks. The red arrows highlight the coexistence of two crystallographic orientations. (b) Identical θ - 2θ XRD patterns of SLs represented in the range between $2\theta = 42^\circ$ and $2\theta = 48^\circ$ for more clarity.

For each superlattices, using the Bragg formula for SLs, we have calculated an average out-of-plane (OP) lattice parameter extracted from the position of the most intense satellite peak¹⁰ (see black squares symbol with line in Figure 2). We have also reported the out-of-plane lattice parameter calculated from the position of the second crystallographic orientation (see red arrows in Figure 1). The average OP lattice parameter is constant for $\Lambda \geq 76 \text{ \AA}$ SLs and is approximately equal to 3.96 \AA (close to BFO's pseudo-cubic bulk value). As observed in the Figure 2, we notice a well-defined change in the OP lattice parameter for $76 \text{ \AA} \leq \Lambda \leq 50 \text{ \AA}$. The decrease of the average OP lattice parameter to values close to 3.94 \AA (close to LFO's bulk value) for small modulation periods $\Lambda \leq 50 \text{ \AA}$, confirms that the SLs undergo a structural change. Note that the additional orientation at $2\theta = 46.15^\circ$ is favored when Λ decreases.

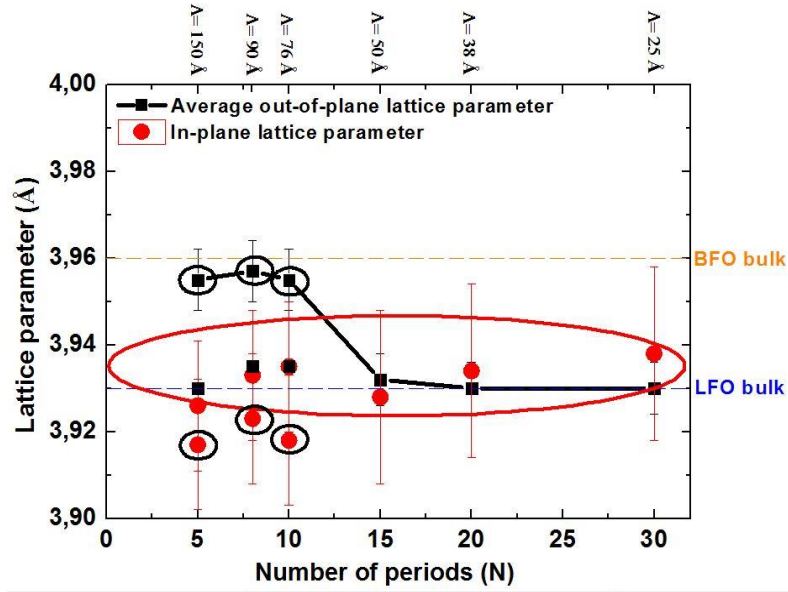


Figure 2: Lattice parameters calculated for all SLs. From θ - 2θ XRD patterns: average out-of-plane lattice parameter (black squares symbol with line) calculated from the position of the most intense satellite peak. The out-of-plane lattice parameter (black squares only) calculated from the position of the second diffraction peak near the main reflection (see red

arrows in Figure 1) coincides with those calculated from the second reflection observed on the RSMs. From RSMs investigations: in-plane lattice parameter calculated from the Q_x position of the different nodes (red dots). Pseudo-cubic bulk values are provided for comparison (dashed horizontal lines).

In order to explore the in-plane structure and domain structure we have performed reciprocal space mapping (RSMs). The (204) and (113) family of planes have been investigated to determine the symmetry of SLs. The RSMs measured for (204), (024), (-204) and (0-24) family of planes (not shown) are similar for all SLs showing an in plane fourfold symmetry. For all SLs, (204) RSMs show an important relaxation of epitaxial strain between the multilayers and the substrate. Figure 3 (a) and (b) exhibits the RSMs obtained for the $\Lambda = 150 \text{ \AA}$ and $\Lambda = 25 \text{ \AA}$ SLs, which are representative for the observed structural change. Two reflections have been observed for larger modulation periods ($\Lambda \geq 76 \text{ \AA}$, see Figure 3 (a)) whereas only one reflection has been detected for smaller periods ($\Lambda \leq 50 \text{ \AA}$, see Figure 3 (b)). The (113) RSMs reveal exactly the same behavior (not shown). According to the number of nodes ((204) and (113) RSMs), rhombohedral or monoclinic distortions have been excluded for all SLs. From these measurements, a pseudo-tetragonal or orthorhombic average structure is therefore inferred. For the $\Lambda \geq 76 \text{ \AA}$ SLs one node (smallest Q_z position) corresponds to the intense diffraction peak at $2\theta = 45.8^\circ$ (see Figure 1) and is associated to an out-of-plane lattice parameter higher than the in-plane lattice parameter (see black circles in Figure 2). The other broad node (highest Q_z position) corresponds to the weak shoulder at $2\theta = 46.15^\circ$ becoming more intense as Λ decreases (red arrows in Figure 1) and is associated with a small difference between out-of-plane and in-plane lattice parameters (red circle in Figure 2). For the $\Lambda \leq 50 \text{ \AA}$ SLs only the node at high Q_z subsists and possesses a large full width at half maximum (FWHM) as observed for

Pnma LFO single layers. Mosaicity and peculiar domain structures with very small lateral correlation lengths can explain the important width of this reflection.

RSM's investigations point out a coexistence of two crystallographic orientations for large periodicities $\Lambda \geq 76 \text{ \AA}$ and only one orientation for small periodicities $\Lambda \leq 50 \text{ \AA}$ (pseudo-tetragonal average structure). These measurements corroborate the θ - 2θ XRD measurements and confirm a change of structure around $76 \text{ \AA} \leq \Lambda \leq 50 \text{ \AA}$. We suppose that the behavior of our SLs is mainly due to the elastic and structural interaction between BFO and LFO layers. **It is important to mention that the STO buffer layer is fully relaxed ($a_{\text{MgO}} = 4.213 \text{ \AA} \gg a_{\text{STO}} = 3.905 \text{ \AA}$). Residual epitaxial strain from MgO substrate remain present but seems not strong enough due to the strain relaxation⁹.**

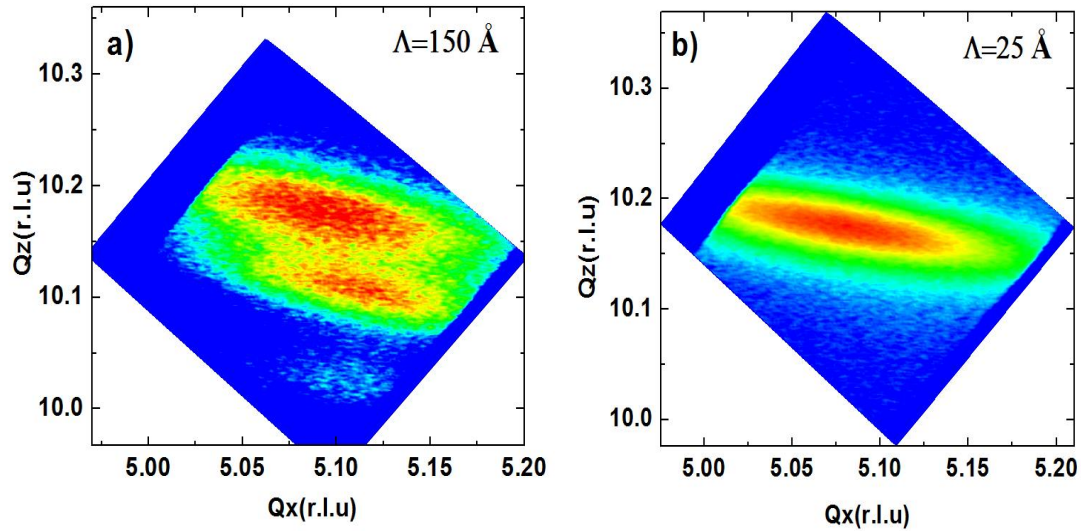


Figure 3: (204) Reciprocal space mapping of the SLs for (a) $\Lambda = 150 \text{ \AA}$ and (b) $\Lambda = 25 \text{ \AA}$.

To get more information about the domain structure of the SLs and better understand the observed structural change, we have undertaken TEM studies on the SL with $\Lambda = 150 \text{ \AA}$ ($N=5$). Periodic nucleation of dislocations (periodicity: 2.85 nm) has been observed at the STO/MgO interface and suggests epitaxial strain relaxation^{9,11} (see supporting information of ref. 9), in agreement with our XRD investigations.

The high resolution TEM image, in Figure 4 (a), shows a very complex nanoscale structure in both layers of the SL. A 45° (with respect to the substrate surface) dense lamellar domains have been detected in the BFO layers (indicated by red square “1” in Figure 4 (a)). The associated Fast Fourier transform (FFT) reveals a periodic modulation of 1.15 nm along the $[011]_{pc}$ direction (at 45° compared to the $(00L)$ growth direction). These 45° nanoscale domains seem to appear only in the BFO layers. Others regions in the BFO layers, as shown in the green square “2” in Figure 4 (a), reveal no domain structures. The LFO layers display horizontal (along $[00L]_{pc}$ direction) and vertical (along $[0K0]_{pc}$ direction) domains, as exhibited in the regions delimited by the blue squares “3” and “4” respectively in Figure 4 (a). The corresponding FFT demonstrate a periodic horizontally and vertically modulated structure of 0.8 nm. Note that similar complex nanoscale domain mixtures have been also observed at the MPB in epitaxial Sm doped BiFeO_3 thin films¹². Figure 4 (b) shows the $[100]$ zone axis selected area diffraction (ZADP) for $\Lambda = 150 \text{ \AA}$. Inspection of this diffraction pattern, allows us to detect $\frac{1}{4} \{011\}$ superstructures spots (indicated by red squares in figure 4 (b)) which closely resembles the well-established antiferroelectric structure in PbZrO_3 ^{12,13}. Such reflections indicate the existence of anti-polar ordering, which probably mainly involves Bi-O atomic displacements. This anti-polar phase has already been observed at the MPB in our investigation of $(\text{BiFeO}_3)_{(1-x)\Lambda} / (\text{LaFeO}_3)_{x\Lambda}$ superlattices⁹, in rare-earth substituted BiFeO_3 ^{2,3,12} and in the $\text{Bi}_{1-x}\text{La}_x\text{FeO}_3$

solid solution^{15,16}. From the comparison of the FFT we can correlate antiferroelectric PbZrO₃-like reflections with the 45° dense lamellar structures observed in the BFO layers. Moreover, the lattice parameter extracted from the $\frac{1}{4}$ {011} spots in the diffraction pattern (Figure 6 (b)) coincides with the period of the BFO lamellar structures and is equal to 1.15 nm. Thus in our SLs, the peculiar domains observed in BFO layers is identified as a PbZrO₃-like structure. At present, in literature the PbZrO₃-like structure detected at the MPB for Bi_{1-x}La_xFeO₃ solid solutions is the subject of many discussions regarding its symmetry^{12,15,17}. This peculiar structure are also discussed for Bi_{1-x}Nd_xFeO₃ system¹⁸ and NaNbO₃^{19,20}.

The diffraction pattern (Figure 4 (b)) reveals also the presence of $\frac{1}{2}$ spots ($\frac{1}{2}$ {001} and $\frac{1}{2}$ {011} as indicated by blue circles) which provides evidence of the existence of a Pnma-like orthorhombic unit cell doubling. From the comparison with the FFT (blue square “3” in Figure 4 (a)), we associate the $\frac{1}{2}$ {001} reflections in the diffraction pattern to the horizontal dense lamellars in the LFO layers. Note that $\frac{1}{2}$ {011} reflections might be explained by twin variants of the orthorhombic Pnma structure, as observed in Sm doped BFO thin films¹¹. The orthorhombic-like unit cell dimension are found to be $a_{pc} \times a_{pc} \times 2a_{pc}$ in Bi_{1-x}La_xFeO₃ thin films² (where a_{pc} is a pseudo-cubic unit cell lattice parameter), explaining the 0.8 nm period estimated in the LFO layers.

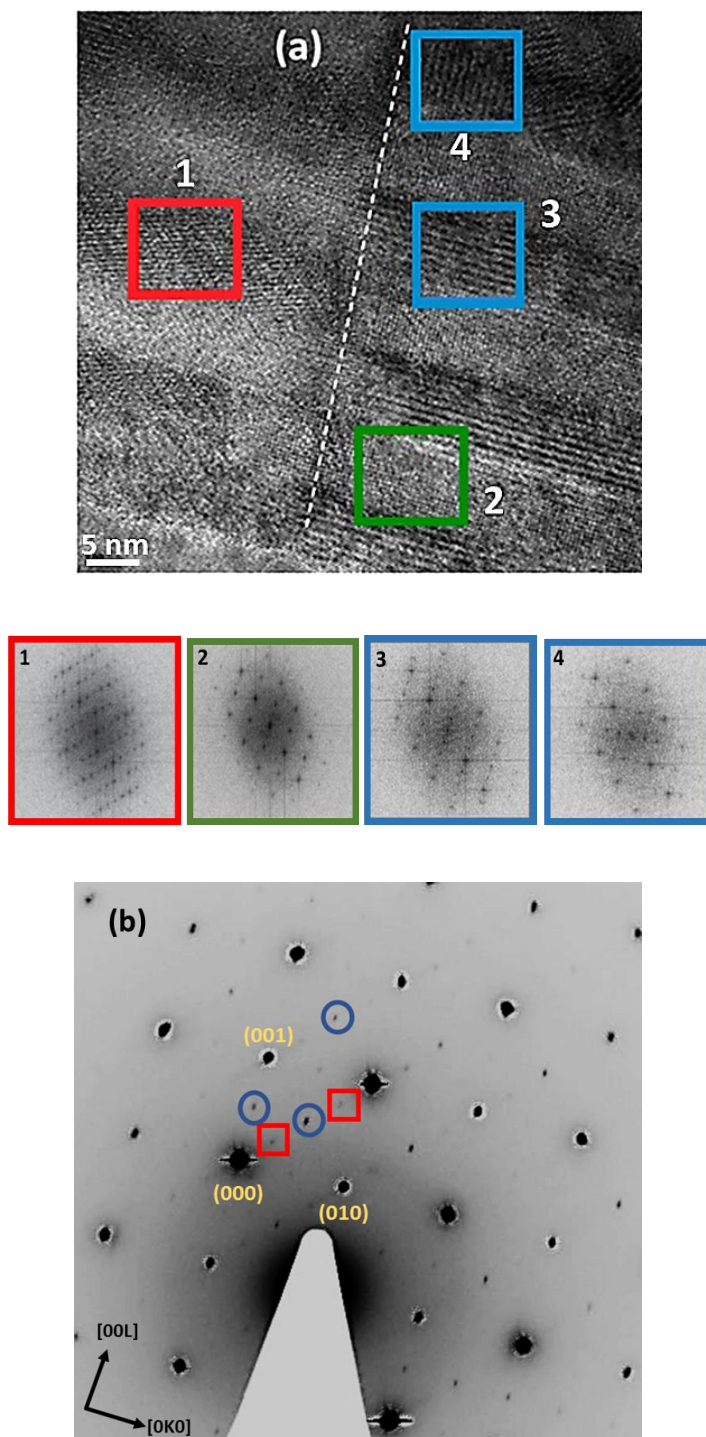


Figure 4: (a) High resolution TEM image for SL with $\Lambda= 150 \text{ \AA}$ ($N=5$). The red square indicates the 45° dense lamellar only present in the BFO layers (periodicity of 1.15 nm), the green square shows any regions which reveal no domain structure in the BFO layers suggesting a pseudo-cubic unit cell. The blue squares highlight the horizontal and vertical

domains in the LFO layers (periodicity of 0.8 nm). Fast Fourier transform (FFT) for each domain is represented below the microscopy image in corresponding colored boxes. (b) [100] ZAPD obtain for $\Lambda=150\text{ \AA}$ SL: red squares and blue circles indicate PbZrO_3 -like reflections ($\frac{1}{4}\{011\}$) and Pnma-like reflections ($\frac{1}{2}\{001\}$ and $\frac{1}{2}\{011\}$) respectively.

To characterize the structural change, a SL with a smaller periodicity ($\Lambda=25\text{ \AA}$) was also investigated by TEM. Inspection of the ZAPD performed on the SL (see Figure 5) allows us to detect only the $\frac{1}{2}\{001\}$ spots (indicated by blue circles). An orthorhombic unit cell with a doubled structure (0.8 nm is estimated) was inferred from these observations. These results highlight the stabilization of the Pnma LaFeO_3 -like structure and corroborate our XRD investigations. Note that the additional modulation observed along the growth direction comes from the presence of satellite peaks. The distance between two successive reflections gives us the value of the SL periods ($\sim 25\text{ \AA}$).

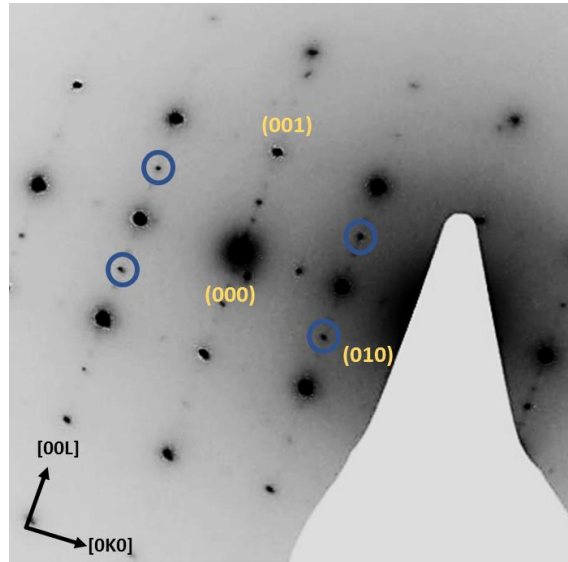


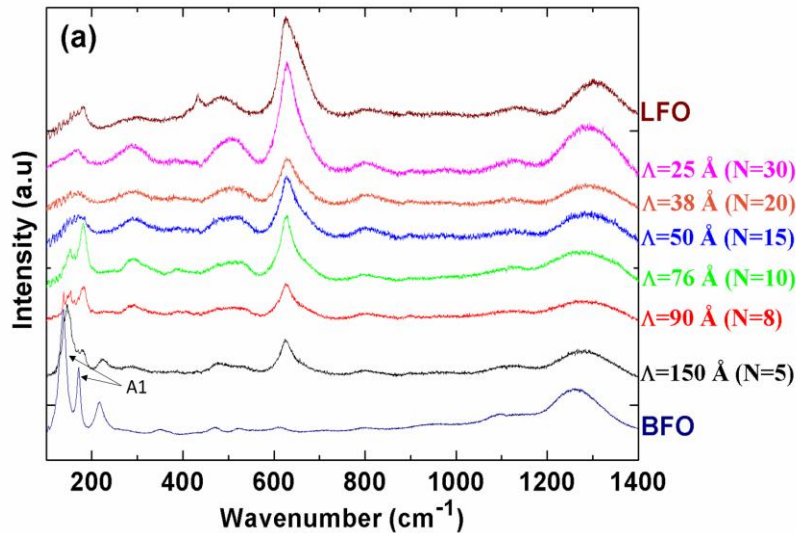
Figure 5: [100] ZAPD obtained for $\Lambda=25\text{ \AA}$ ($N=30$) SL showing only Pnma-like reflections ($\frac{1}{2}\{001\}$ indicated by blue circles).

TEM studies corroborate the XRD measurements and reveal a complex structural coexistence occurring in $(\text{BiFeO}_3)_{0.5\Lambda}/(\text{LaFeO}_3)_{0.5\Lambda}$ SL for $\Lambda = 150 \text{ \AA}$. The two different crystallographic orientations observed by X-ray diffraction most likely correspond to the two different structures observed by TEM: PbZrO_3 -like confined to the BFO layers and Pnma -like in the LFO layers.

To better understand these structures, all SLs have subsequently been investigated by Raman spectroscopy. Figure 6 exhibits the room temperature Raman spectra for parallel $Z(\text{XX})\bar{Z}$ and crossed $Z(\text{XY})\bar{Z}$ geometries. To do a direct comparison, Raman spectra of BFO and LFO single films are also displayed. The BFO thin film Raman spectra is typical of a R3c rhombohedral phase characterized by the two low frequency A_1 modes around 138 cm^{-1} and 170 cm^{-1} respectively. These two phonons are characteristic of the R3c polar state in BFO bulk and thin films and provide a good spectral signature for any symmetry change. The Raman spectra obtained for the $\Lambda = 150 \text{ \AA}$ ($N=5$) SL shows a strong similarity with the BFO thin film Raman spectra. Indeed, two peaks below 200 cm^{-1} are reminiscent of the BFO A_1 low frequency modes. However, in superlattices significant mode hardening is observed as these phonons appear at higher frequencies around 150 cm^{-1} and 180 cm^{-1} . This hardening suggests the possibility of an important modification in Bi cations displacement. This aspect of this Raman spectra (different from $\Lambda = 90 \text{ \AA}$ and $\Lambda = 76 \text{ \AA}$) supports the existence of the complex nanoscale domain orientation detected by TEM studies. As we decrease the modulation period Λ (case for $\Lambda = 90 \text{ \AA}$ and $\Lambda = 76 \text{ \AA}$), we observe a change in relative intensity between these two low frequencies modes (Figure 6(a)). Indeed, the phonons at 180 cm^{-1} being more intense than the one at 150 cm^{-1} (opposite is observed on the BFO film). These Raman spectra closely resemble the Raman spectra obtained near the MPB for $\text{Bi}_{1-x}\text{La}_x\text{FeO}_3$ solid solution ($0.2 \leq x \leq 0.5$) by Bielecki *et al.*¹⁶. For these

compositions, the authors suggest the existence of a PbZrO_3 antiferroelectric-like state. It is believed that this antiferroelectric distortion acts like a structural bridge between rhombohedral $R3c$ and orthorhombic Pnma phases. Raman selection rules predict an important increase of Raman phonon bands when going from the $R3c$ to the PbZrO_3 -like symmetries (Pbam or Pnam). However, the presence of large bands does not allow us to separate the different contributions and it is difficult to identify the exact number of phonons.

For superlattices with smaller periodicity $\Lambda \leq 50 \text{ \AA}$, the global shape of these Raman spectra closely resembles that of the LFO thin film with the Raman spectra clearly different to the others (for example the Raman spectra for $\Lambda \geq 76 \text{ \AA}$). The two intense low frequency modes completely disappear, and give rise to large bands at the same frequencies compared to the LFO thin film. From these results, it is believed that orthorhombic Pnma phase is stabilized for $\Lambda \leq 50 \text{ \AA}$.



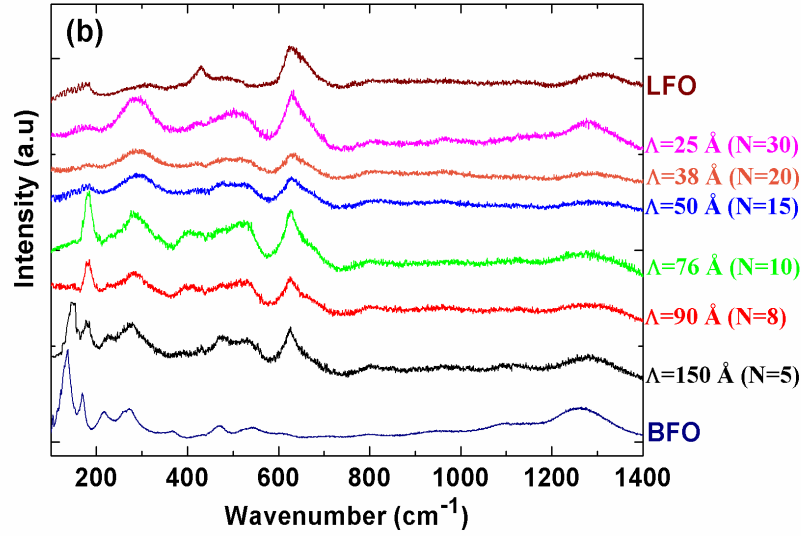


Figure 6: Room temperature Raman spectra of $(\text{BiFeO}_3)_{0.5\Lambda}/(\text{LaFeO}_3)_{0.5\Lambda}$ superlattices in (a) parallel $Z(\text{XX})\bar{Z}$ and (b) crossed geometry $Z(\text{XY})\bar{Z}$.

In brief, Raman investigations allow us to distinguish SLs with larger ($\Lambda \geq 76 \text{ \AA}$) and smaller ($\Lambda \leq 50 \text{ \AA}$) periodicity. On one hand for $\Lambda \geq 76 \text{ \AA}$, spectral signatures are detected which support the existence of antiferroelectric ordering. On the other hand, for $\Lambda \leq 50 \text{ \AA}$, anti-polar ordering vanishes completely and signatures of orthorhombic Pnma -like phase are observed. These measurements corroborate our TEM and XRD studies which exhibits a structural change around $76 \text{ \AA} \leq \Lambda \leq 50 \text{ \AA}$. To verify the impact of such structural modifications on the magnetic properties, vibrating sample magnetometry was performed at room temperature.

Figure 7 presents the room temperature magnetic ($M(H)$) loops obtained on five superlattices measured with the field applied in the plane of the samples. The slim hysteresis loops show weak ferromagnetism independent of the superlattice periodicity with the magnetization at saturation varying between 15 and 70 $\text{emu}\cdot\text{cm}^{-3}$. These values are superior to those observed in thin films of pure BFO and LFO and this could be explained by the presence of impurities, oxygen vacancies and interdiffusion at the BFO/LFO interfaces. Indeed enhanced magnetization has been shown for $(\text{Bi}_{1-x}\text{La}_x)\text{FeO}_3$ thin film solid solution ($x=0.1, 0.2$)^{21,22,23}. We must stress that all samples have been synthesized under the same growth conditions and thus the same amount of impurities should be expected to be present for the whole set of samples. Therefore, if we consider the small enhancement in magnetization of 15 $\text{emu}\cdot\text{cm}^{-3}$ to arise solely from impurities this suggests that only very small amount of impurities are present in our SLs consistent with our diffraction analysis. No trend could be detected with the number of periods which suggests a similar antiferromagnetic order with a weak ferromagnetic component consistent with strained BFO and LFO thin films. It is important to note that strained BFO thin films do not exhibit spin cycloid magnetic ordering (which is very sensitive to applied strain) and spin homogenization can contribute to the observed enhanced magnetization at saturation. Temperature dependent magnetic measurements (VSM and magnetic susceptibility) are currently under progress and will be the subject of another report.

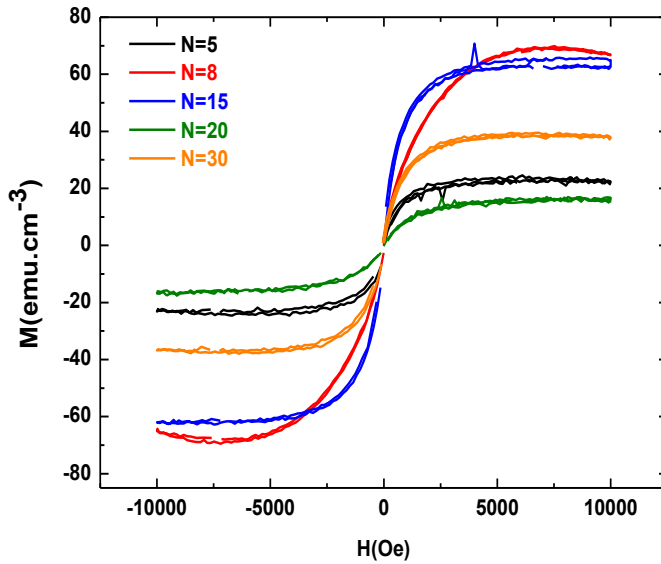


Figure 7: In plane room temperature magnetic hysteresis loops (M versus H) of the BFO/LFO superlattices. Diamagnetic contribution of the substrates have been corrected.

In order to establish the effect of strain on phase stability and to better understand the exact origin of the antiferroelectric phase we have carried out temperature dependent X-ray diffraction measurements.

This study consisted to measuring the θ - 2θ diffraction pattern over a wide temperature range in order to extract the average out-of-plane lattice parameters as a function of temperature. For all samples, the expected linear thermal dilatation was observed for the MgO substrate (results not shown). Figure 8 (a) displays average out-of-plane lattice parameters from room to high temperature (650°C) for each of the superlattices investigated.

SLs with larger periodicity ($\Lambda \geq 76 \text{ \AA}$) show an important anomaly at high temperature resulting in a significant decrease of the average out-of-plane lattice parameter. However, SLs with smaller periodicity ($\Lambda \leq 50 \text{ \AA}$) only exhibit linear dilatation versus temperature. These results confirm once more the difference between SLs with larger and smaller modulation periods, as observed in our XRD, TEM and Raman spectroscopy data. Structural anomalies are only observed for $\Lambda \geq 76 \text{ \AA}$ SLs, for which we provide evidence of an antiferroelectric-like state (see TEM and Raman investigations). These anomalies are therefore correlated to the presence of an antiferroelectric PbZrO_3 -like structure in the BFO layers. According to the tendency of BFO to adopt a paraelectric Pnma phase at high temperature, we associate these anomalies with a structural phase transition from an antiferroelectric-like to a paraelectric-like state.

For the others SLs ($\Lambda \leq 50 \text{ \AA}$), the lack of a transition suggests the stabilization of the paraelectric Pnma -like state across the whole temperature range studied. These results support our interpretation of Pnma -like symmetries for these SLs, in agreement with our XRD TEM and Raman investigations.

To determine the exact temperature of the phase transition for the $\Lambda \geq 76 \text{ \AA}$ SLs, we corrected the out-of-plane lattice parameter from the linear paraelectric contribution at high temperature, as presented in Figure 8 (b)²⁴. This correction allows us to better observe the anti-polar distortion, below the critical temperature. We clearly see a shift of the critical temperature, T_c , (antiferroelectric to paraelectric) to lower temperatures as the modulation period Λ decreases. In this set of SLs, the BFO ratio is equivalent to the LFO ratio in each period Λ , thus for small periodicities the BFO thickness in the period is less important than for the SLs with large periodicity. We can, therefore, infer a scaling of T_c with the BFO

thickness in the period, as already observed by Rispens *et al.* in BFO/LFO SLs⁸. In our SLs the global strain state may explain this peculiar behavior (shift of T_c). Nevertheless, as observed by Infante *et al.* the octahedral rotation/tilt degrees of freedom may play an important role in the accommodation of strain and in the thermal phase stability²⁴.

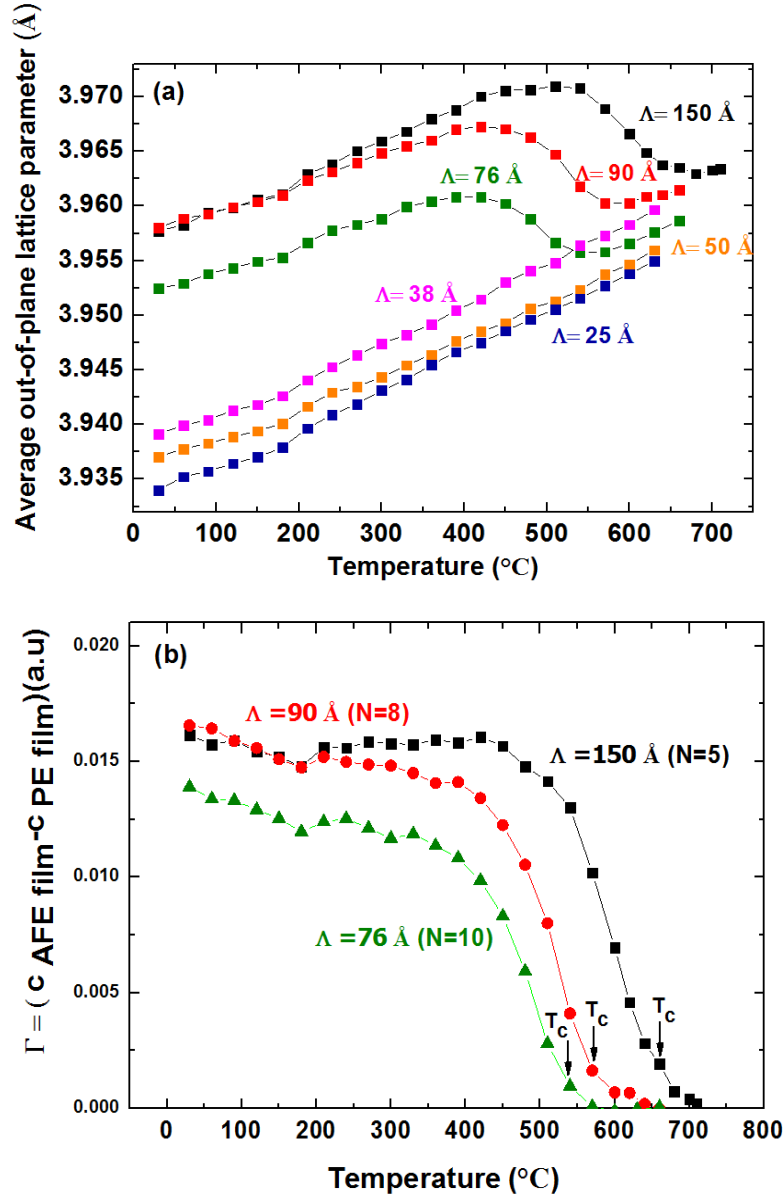


Figure 8: (a) Average out-of-plane lattice parameter versus temperature for all $(\text{BiFeO}_3)_{0.5\Lambda}/(\text{LaFeO}_3)_{0.5\Lambda}$ superlattices and (b) corrected out-of-plane lattice parameter versus temperature for only $\Lambda \geq 76$ Å SLs showing a structural phase transition.

Note that we also observe a deviation from linearity close to 200°C for all SLs. This anomaly has already been detected in BFO thin films and bulk materials and interpreted as spin-lattice coupling. Indeed, the authors pointed out a modification of the magnetic structure involving Fe-O bond length changes^{22,23}.

Conclusion

In this study, we have investigated the structural behavior of BiFeO₃ / LaFeO₃ superlattices grown on cubic MgO (100) substrates as a function of modulation period Λ . These investigations allow us to highlight a competition between antiferroelectric PbZrO₃-like and Pnma-like states that depends strongly on the BFO thickness in the period in the SLs. These different peculiar domain states are revealed using a combination of XRD, TEM and Raman spectroscopy. The exact origin of such an antiferroelectric-like state is not yet determined. BFO is expected to be under an in-plane compressive strain applied from the LFO layers in the studied SLs and according to the literature a so-called super-tetragonal phase is therefore expected in BFO. The observed PbZrO₃-like structure clearly calls for additional factors and oxygen octahedral rotation/tilt compatibilities at heterointerfaces may contribute to the phase stability in the SLs^{24,27}.

The room temperature magnetic properties suggest an antiferromagnetic ordering with weak ferromagnetism. Similarly to strained BFO thin film the spin cycloid is expected to disappear and spin homogenization may contribute to the enhanced ferromagnetic response in the SLs.

Temperature dependent X-ray diffraction shows a tuning of the antiferroelectric to paraelectric phase transition. Thermal stability of the antiferroelectric state is explained by a strong interplay between strain, octahedral tilt and Bi anti-polar ordering.

Recently first principles theory predicts nanoscale twinned phases in BFO due to competing instabilities (antiferrodistortive versus ferroelectric ordering)²⁰ while another model points out the role of flexoelectric interaction in these modulated phases.⁵ The observed MPB like state is probably explained by these models and such an MPB like state could be expected to host a variety of remarkable properties (piezoelectric and magnetoelectric) currently under investigations.

References:

1. Sando D., Barthélémy A. & Bibes M., *J. Phys. Condens. Matter* 26, 473201 (2014).
2. Kan D., Cheng C.-J., Nagarajan V. & Takeuchi I. C, *J. Appl. Phys.* 110, 014106 (2011).
3. Kan D. et al., *Adv. Funct. Mater.* 20, 1108–1115 (2010).
4. Arnold D., *IEEE Transactions on Ultrasonics, Ferroelectrics, and Frequency Control*, 62, 1, 62-82 (2015).
5. Borisevich A. Y. et al., *Nat. Commun.* 3, 775 (2012).
6. Ranjith R., Kundys B. & Prellier W., *Appl. Phys. Lett.* 91, 222904 (2007).
7. Maran R. et al., *Phys. Rev. B* 90, 245131 (2014).
8. Rispen G. et al., *Phys. Rev. B* 90, 104106 (2014).
9. Carcan B. et al., *Advanced Materials Interfaces* 4 (11), 1601036 (2017).
10. Yuzyuk Y. I. et al., *J. Appl. Phys.* 116, 184102 (2014).

11. Tse Y. Y., McMitchell S. R. C., Jackson T. J., Jones I. P. & Genc A., *Thin Solid Films*, 520, 3440–3447 (2012).
12. Cheng C.-J. et al., *Phys. Rev. B* 80, 014109 (2009).
13. Boldyreva K. et al., *J. Appl. Phys.* 102, 044111 (2007).
14. Sawaguchi E., Maniwa H. & Hoshino S., *Phys. Rev.* 83, 1078–1078 (1951).
15. Troyanchuk I. O. et al., *Phys. Rev. B* 83, 054109 (2011).
16. Bielecki J. et al., *Phys. Rev. B* 86, 184422 (2012).
17. Rusakov D. A. et al., *Chem. Mater.* 23, 285–292 (2011).
18. Karimi S., Reaney I., M. Levin I., & Sterianou I., *Appl. Phys. Lett.* 94, 112903 (2009).
19. Peel M. D., Thompson S. P., Daoud-Aladine A., Ashbrook S. E., Lightfoot P., *Inorg. Chem.* 51, 6876–6889 (2012).
20. Prosandeev S., Wang D., Ren W., Íñiguez J., Bellaiche L., *Adv. Funct. Mater.* 23, 234–240 (2013).
21. Lee et al. *Appl. Phys. Lett.* 86, 222903 (2005).
22. Hong Liu et al., *Journal of Advanced Dielectrics* Vol. 1, No. 3363_367 (2011).
23. W.-H. Kim and J. Y. Son *Appl. Phys. Lett.* 103, 132907 (2013)
24. Infante, I. C. et al. *Phys. Rev. Lett.* 105, 057601 (2010).
25. Haumont, R. et al. *Phys. Rev. B* 78, 134108 (2008).
26. Toupet H., Le Marrec F., Lichtensteiger C., Dkhil B., Karkut M. G., *Phys. Rev. B* 81, 140101 (2010).

27. Vailionis, A. et al., Phys. Rev. B 83, 064101 (2011).

28. Tagantsev A. K., et al. Nat. Commun. 4, 2229 (2013).